Altering strength and plastic deformation behavior via alloying and laminated structure in nanocrystalline metals

Article *in* Materials Science and Engineering A · May 2015

DOI: 10.1016/j.msea.2015.05.009

CITATIONS
0

READS
46

5 authors, including:

Chao Gu
Xi'an Jiaotong University
5 PUBLICATIONS **2** CITATIONS
SEE PROFILE

Fei Wang
Xi'an Jiaotong University
54 PUBLICATIONS **266** CITATIONS
SEE PROFILE

Tian Jian Lu
Xi'an Jiaotong University
551 PUBLICATIONS **8,635** CITATIONS
SEE PROFILE

Ke-Wei Xu
Xi'an Jiaotong University
495 PUBLICATIONS **4,334** CITATIONS
SEE PROFILE

Materials Science & Engineering A 640 (2015) 24–32

Contents lists available at ScienceDirect

Materials Science & Engineering A

journal homepage: www.elsevier.com/locate/msea

Altering strength and plastic deformation behavior via alloying and laminated structure in nanocrystalline metals

C. Gu [a], F. Wang [b,*], P. Huang [a,*], T.J. Lu [b,c], K.W. Xu [a]

[a] State Key Laboratory for Mechanical Behavior of Material, Xi'an Jiaotong University, Xi'an 710049, China
[b] State Key Laboratory for Strength and Vibration of Mechanical Structures, Xi'an Jiaotong University, Xi'an 710049, China
[c] MOE Key Laboratory for Multifunctional Materials and Structures, Xi'an Jiaotong University, Xi'an 710049, China

ARTICLE INFO

Article history:
Received 16 February 2015
Received in revised form
29 April 2015
Accepted 3 May 2015
Available online 14 May 2015

Keywords:
Alloying
Interface
Nanocrystalline
Nanoindentation
Deformation mechanism

ABSTRACT

Nanoindentation and electron microscope techniques have been performed on sputtering deposited monolayered nanocrystalline CuNb and multilayered CuNb/Cu thin films. Microstructural features, hardness and surface morphologies of residual indentation have been evaluated to identify the effects of alloying and laminated structure on strength and plastic deformation behavior of nanocrystalline metals. By altering the content of Nb in CuNb alloy and adding crystalline Cu layers into CuNb alloy, the volume fraction of amorphous phase in CuNb alloy and interface structures changed dramatically, resulting in various trends that are related to hardness, indentation induced pileup and shear banding deformation. Based on the experimental results, the dominant deformation mechanisms of the CuNb and CuNb/Cu thin films with various Nb contents were proposed and extended to be discussed.

1. Introduction

Nanocrystalline (NC) metals with novel mechanical properties have been the focus of research efforts over the past few decades. NC metals usually exhibit a higher strength compared with their coarse grain counterparts, but a lower ductility that greatly limits their engineering application. In general, the limited ductility in NC metals mainly attributes to lack of available strain accommodation processes and low work hardening capability [1]. Therefore, tremendous efforts have been applied to improve the ductility of NC metals by introducing nanotwins [2,3] or fabricating metals with binomial grain size distribution [4,5].

Other than the aforementioned methods, nanoscale multilayered structure has also been proved to be an effective way to achieve desirable strength and ductility of metallic materials. Specifically, the strength and ductility of metallic multilayers were attributed by modulation periods and the choices of the constituent layers [6]. Generally, the hardness of multilayer thin films with equal individual layer thickness (h) will increase with decreasing h. The dominated strengthening mechanism of these multilayers has been systematically studied. Hall–Petch (H–P) relation, the confined layer slip (CLS) model and the interface crossing model had been successfully applied on explaining the strength of crystalline/crystalline multilayer thin films with h ranging from micrometer to a few nanometers [7]. The structure and strength of the interfaces between the heterogeneous phase layers have been proposed to play an important role in determining the deformation behavior of the multilayers. However, the ductility is still strictly limited in most of the multilayer systems with equal individual layer thickness. In recent years, by adding very thin crystalline layers into amorphous or crystalline phases, the ductility of these laminate structure materials has been effectively improved [8–10] by the existence of crystalline/amorphous interfaces (CAIs) or crystalline/crystalline interfaces.

Alloying is another way to effectively enhance the strength and thermal stability for pure NC metals [11]. By alloying, both grain size and stacking fault energy of NC metals should decrease, resulting in high strength and strong twinning formation ability. Moreover, the volume fraction of amorphous phase in NC alloys could be increased by increasing solute atoms content, leading to plastic deformation transformed from NC-like to amorphous-like behavior [12], i.e., from dislocation dominated to shear bands (SBs) dominated. This characteristic of nanocrystalline alloys provides an effective way to systematically study the deformation behavior of both crystalline and amorphous phases in an identical alloy system. Furthermore, the structure of alloy phase could affect the interface structure when adding heterogeneous phase layers into the monophase alloy. As mentioned above, while the interface structure could strongly affect the deformation mechanisms of the laminated structured thin films, the specific impact of the interface

* Corresponding authors. Tel.: +86 29 82663869; fax: +86 29 82663453.
E-mail addresses: wangfei@mail.xjtu.edu.cn (F. Wang), huangping@mail.xjtu.edu.cn (P. Huang).

http://dx.doi.org/10.1016/j.msea.2015.05.009
0921-5093/

with different structures could also be systematically studied in the alloy system.

In the present study, by considering the effects of both alloying and multilayered structure, the microstructure and mechanical properties of CuNb alloy thin films with and without crystalline Cu layers were examined mainly by nanoindentation test and electron microscope analysis, to explore the effects of interface structure formed between CuNb and Cu layers on the strength and plastic deformation behavior.

2. Experimental details

CuNb alloy thin films with various Nb contents f_{Nb} were deposited on single crystal Si substrate by magnetron sputtering under argon pressure of 0.3 Pa at room temperature. Direct current (DC) and radio frequency (RF) power co-sputtering pattern were used for CuNb depositing, in which RF power with a fixed value of 100 W for Cu deposition, while DC power of 20 W, 60 W and 100 W were used for Nb deposition. The layer thicknesses of all the CuNb thin films were maintained as 1500 nm. Energy dispersive spectrometer (EDS) result showed that Nb contents were 9.3 at%, 22 at% and 36 at% for the CuNb alloys deposited under DC powers of 20 W, 60 W and 100 W, respectively.

Other than the CuNb alloy, multilayered $CuNb_x$/Cu (x=9.3 at%, 22 at% and 36 at%) thin films, in which the contents of Nb in CuNb layers were identical to that of the monophase CuNb alloys, were also prepared by alternatively depositing a 140 nm CuNb layer and a 10 nm Cu layer of 10 cycles. Thus the total layer thicknesses were also 1500 nm for all the $CuNb_x$/Cu multilayers. In addition, the interface structures of the three kinds of multilayers varied with the Nb content, the detailed information of the monolayer $CuNb_x$ and multilayer $CuNb_x$/Cu samples is shown in Fig. 1. Structural characterization of Cu, Nb and CuNb alloy thin films was performed by X-ray diffraction (XRD, using a D3290 PANalyticalX'pert PRO with Cu-Kα radiation) analysis, and the microstructural features of CuNb and CuNb/Cu samples were examined by using high-resolution transmission electron microscopy HRTEM (JEOL JEM-2100F operating at 200 kV). The mechanical properties were investigated by using a MTS Nanoindenter XP system (MTS, Inc.) under Continuous Stiffness Measurement (CSM) mode. The radius of the Berkovich tip was calibrated to be around 50 nm, and the applied strain rate was set as a constant of 0.05 s^{-1}. The residual indentation morphologies of each sample were characterized by using scanning electron microscope (SEM).

3. Results

3.1. Microstructural features

3.1.1. Monophase CuNb alloy

Fig. 2 shows the XRD patterns of pure Cu, Nb and CuNb alloys with various Nb contents. Specifically, Fig. 2(a) indicates that CuNb9.3 at% alloy exhibited nearly identical diffraction peaks as pure Cu with face-centered cubic lattice structure, indicating that Nb atoms may nearly completely dissolve in Cu lattice as substitutional solid solution and no precipitated phase was formed. As f_{Nb} increased, the diffraction peaks of CuNb22 at% and CuNb36 at% moved to lower angle range that is close to the angles corresponding to Nb diffraction peaks. Detailed and magnified diffraction patterns of CuNb9.3 at%, CuNb22 at% and CuNb36 at% are shown in Fig. 2(b). Although the sharp peak of Cu(111) at 43.5° appeared in CuNb9.3 at% alloy, broad hump appeared roughly around angle of 40.5° in CuNb22 at% and Cu(200) and Cu(311) peaks disappeared except for a relatively stronger Cu(220) peak at 73.0°. For CuNb36 at% alloy, similar broad hump centered at 41° appeared and Cu(220) peak was weakened. Therefore, the diffraction patterns shown in Fig. 2 indicate that the CuNb alloys transformed from crystal-like to amorphous-like lattice structures as f_{Nb} increased.

3.1.2. $CuNb_x$/Cu multilayers

Cross-sectional TEM images of $CuNb_x$/Cu multilayers are shown in Fig. 3. For CuNb9.3 at%/Cu, the bright field and dark field images shown in Fig. 3(a) and (b), respectively, indicate that adding Cu layers could be clearly observed as pointed by white arrows. The diffraction pattern in the upper left of Fig. 3(a) shows that the lattice parameter of CuNb9.3 at%/Cu is the same as pure Cu, and is consistent with XRD results shown in Fig. 2. In Fig. 3(b), a single grain in CuNb9.3 at%/Cu is marked by the yellow circle curve, which indicates that the in-plane grain size of CuNb9.3 at%/Cu is about 50 nm. Detailed HRTEM image of the yellow dashed box in Fig. 3(b), which

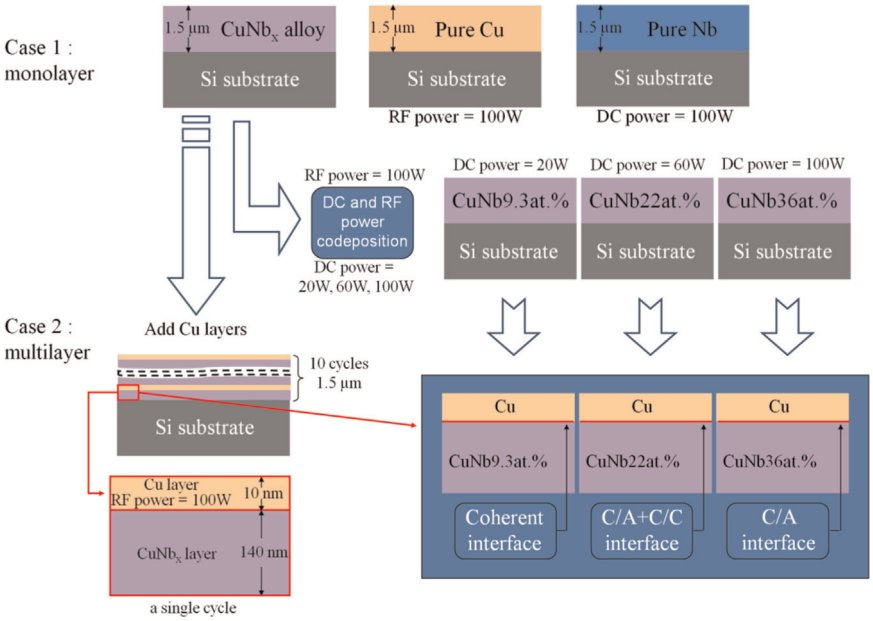

Fig. 1. Schematic diagram of the fabrication of the monolayer $CuNb_x$ films and multilayer $CuNb_x$/Cu films with different interface structures.

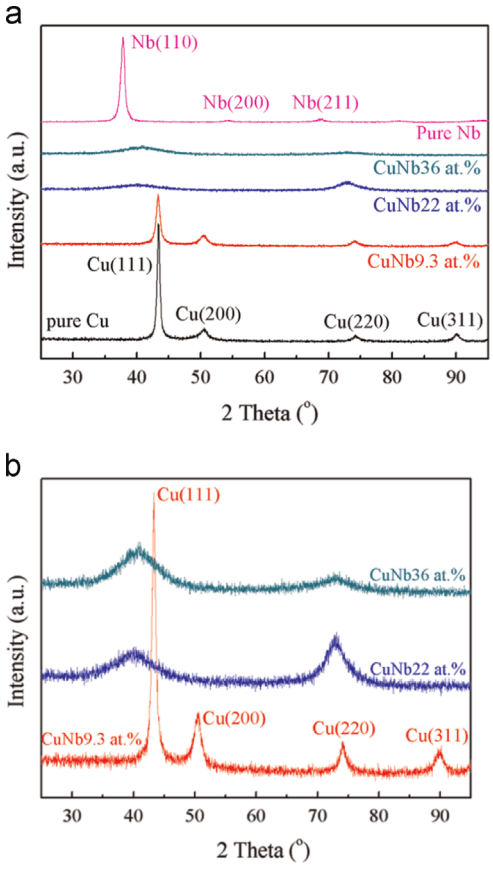

Fig. 2. XRD patterns of (a) pure Cu, Nb, CuNb alloys and (b) $CuNb_x$/Cu thin films.

contains CuNb alloy layers on both sides of adding Cu layer, is shown in Fig. 3(c). Interfaces of Cu and CuNb alloy are highlighted by yellow dotted lines in Fig. 3(c). IFFT image of dashed box① shows that the GBs width of CuNb9.3 at% alloy was only a few atoms length. By getting the IFFT image of the yellow dashed box② showing the atom arrangement around interface, the growth of coherent interface between Cu and CuNb could be clearly observed. In area surrounded by the green dash lines, stacking faults were observed in both Cu layer and CuNb alloys. Previously, experimental evidences have been provided that twins or stacking faults initiated in Cu layer could penetrate (across) into Ni (high SFE metal) or Co (low SFE metal) layer in Cu/Ni [13] and Cu/Co [14] multilayers, respectively. Therefore, considering the growth direction is from the top to the bottom in the figure, stacking faults might initially form in Cu layer and then across the interface to continually grow to CuNb layer.

Fig. 3(d) and (e) shows the bright field and dark field images, respectively, of CuNb22 at%/Cu. The average sizes (~6 nm) of the equi-axed grains in Cu and CuNb alloys were almost unanimously made of Cu layers which are difficult to be distinguished from the bright field image in Fig. 3(d). However, Cu layers could be clearly discerned from the dark field images shown in Fig. 3(e) as indicated by the white arrows. Interestingly, amorphous halo appeared in the diffraction pattern of CuNb22 at%/Cu in the inset of Fig. 3(d). This is consistent with the observation in the inset showing the microstructure of CuNb alloy besides Cu layer in Fig. 3(f), in which crystal CuNb grains within blue dotted ellipses were surrounded by amorphous areas [could be considered as thicker grain boundary (GB)] in width of about 3 nm. In addition, the interfaces between Cu and CuNb22 at% alloys highlighted by yellow dotted lines in Fig. 3 (f) were found to be quite different from those in CuNb9.3 at%/Cu, as two types of interfaces (termed as T1 and T2 interface hereafter) were formed in CuNb22 at%/Cu. As shown in Fig. 3(f), T1 interfaces were the areas between crystalline Cu and CuNb layers, while T2 interfaces were the regions between crystalline Cu layer and amorphous CuNb layer.

For CuNb36 at%/Cu alloy, the two constituent layers could be easily identified in both bright and dark field TEM images shown in Fig. 3(g) and (h), respectively. Specifically, a much wider amorphous halo than that in CuNb22 at%/Cu alloy appeared as shown in the inset of Fig. 3(g). The HRTEM image shown in Fig. 3 (i) indicates that the microstructure of CuNb36 at% consists of two parts: amorphous CuNb and crystal CuNb particles with grain size of about 4 nm evenly spread in amorphous phase. Under this microstructural circumstance, only T2 interfaces, i.e., the interfaces between crystalline Cu and amorphous CuNb layers were observed. Moreover, consistent with CuNb22 at%/Cu, stacking faults were found in Cu layer. The inset of Fig. 3(i) shows a few but existed areas in Cu layer, in which the disorder atomic arrangement was quite different from amorphous structure. The FFT image of the region in the yellow dotted box indicates that the atomic arrangement is a confusion in this kind of regions. However, the diffraction pattern, presented in the form of spots rather than halo, indicates that the structure of this particular region is still crystalline-like.

In brief, the aforementioned experimental results clearly indicate that f_{Nb} could effectively change the microstructural features of CuNb/Cu multilayers. Then, the effects of the microstructural features on mechanical properties of CuNb/Cu multilayers will be presented and discussed in the following sections.

3.2. Hardness

Nanoindentation hardness as a function of f_{Nb} for $CuNb_x$ and $CuNb_x$/Cu samples is shown in Fig. 4, in which all the hardness values of $CuNb_x$ and $CuNb_x$/Cu fall in the range from 3.69 GPa for pure Cu to 7.75 GPa for pure Nb. For CuNb thin films, two linear regions were identified as the hardness increased rapidly at the f_{Nb} ranging from 0 to 22 at% while the hardness increased relatively slower when f_{Nb} was getting higher.

At first glance, the hardness of CuNb/Cu multilayers followed the trend derived for CuNb films as mentioned above. However, close inspection indicated that the effects of adding Cu layers into CuNb films were quite different from each other. The hardness differences, i.e., $\Delta H = H_{CuNb/Cu} - H_{CuNb}$, between $CuNb_x$/Cu and $CuNb_x$ are shown in the inset image of Fig. 4. Although the hardness of Cu is lower than CuNb alloy, strengthening effect, weakening effect and event nearly non-effect were observed by adding Cu layers. Specifically, even the thickness and volume fraction of Cu layers in different CuNb/Cu samples are identical, ΔH varies widely from ~0.10 GPa to ~1.38 GPa.

3.3. Indention morphology

The SEM images of the residual indentations of $CuNb_x$ and $CuNb_x$/Cu multilayers are shown in Fig. 5, in which pileups and cracks are observed for pure Cu and Nb in Fig. 5(a) and (e), respectively. More pronounced pileups were formed in CuNb9.3 at% [Fig. 5(b)] and multiple shear bands (SBs) were observed in CuNb22 at% [Fig. 5(c)] and CuNb36 at% [Fig. 5(d)]. Similar trend was observed for $CuNb_x$/Cu multilayers as the f_{Nb} increases, i.e., pileups appeared at Nb content of 9.3 at% while SBs were identified around residual indentations at Nb contents of 22 at% and 36 at%. It is noteworthy that the extent of pileups became more pronounced from pure Cu [Fig. 5(a)] to CuNb9.3 at% [Fig. 5(b)] and further to CuNb9.3 at%/Cu [Fig. 5(f)]. In addition, more SBs appeared in CuNb22 at%/Cu [Fig. 5(g)] and CuNb36 at%/Cu [Fig. 5(h)] than that in CuNb22 at% [Fig. 5(c)] and CuNb36 at% [Fig. 5(d)], respectively.

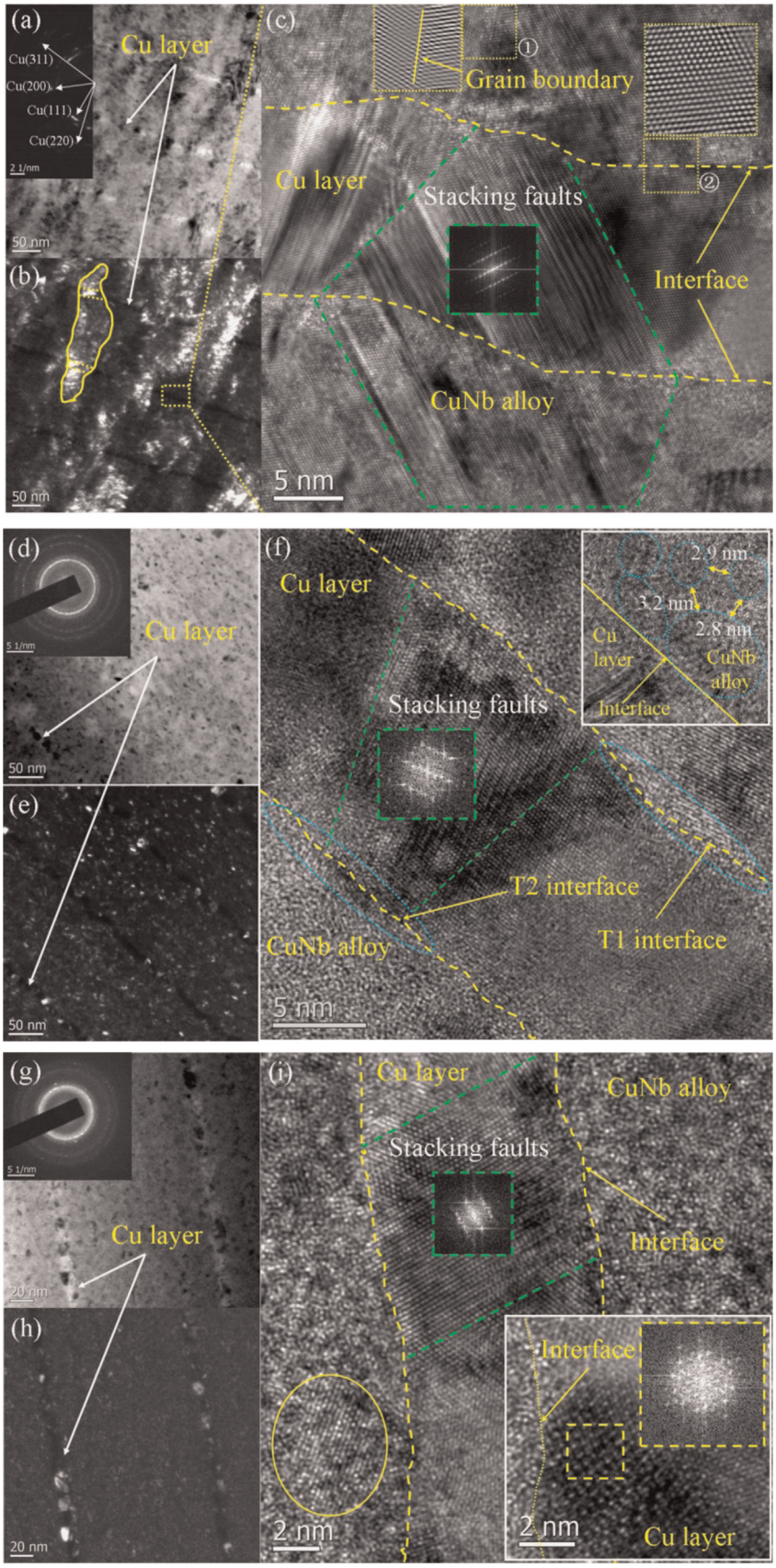

Fig. 3. Cross-sectional HRTEM images of (a)–(c) CuNb9.3 at%/Cu, (d)–(f) CuNb22 at%/Cu and (g)–(i) CuNb36 at%/Cu. See the text for detail. (For interpretation of the references to color in this figure, the reader is referred to the web version of this article.)

4. Discussion

4.1. Strengthening mechanism

As shown in Fig. 4, the hardness of both $CuNb_x$ and $CuNb_x$/Cu increases with increasing f_{Nb}. In the following, the deformation mechanisms of $CuNb_x$ and $CuNb_x$/Cu will be separately discussed in terms of evaluating microstructural features demonstrated in Fig. 3.

4.1.1. Strengthening mechanism of CuNb alloy

For $CuNb_x$ thin films, increased hardness may derive from two reasons: grain size reduction and increased amorphous content. Previously, Hall–Petch and inverse Hall–Petch relationships were used to interpret the strengthening mechanism of nanocrystalline metals as grain size reduced to nanoscale [15]. The variation trend of hardness deviated from the Hall–Petch relationship always corresponding to the deformation mechanism transform from dislocation-mediated process to GBs mediated one [16]. In the present study, the microstructure of $CuNb_x$ thin films changed from nanocrystalline to tiny nano-particles embedded into amorphous matrix which is the same as NiW alloys that are shown in Rupert et al.'s study [17]. As the volume fraction of amorphous phase will increase with increasing Nb content, the strengthening mechanism of $CuNb_x$ thin films will be divided into two parts, i.e., dislocation dominated and amorphous phase dominated. There is a critical value of f_C, below which the GB width was only 1–2 atoms, where no amorphous phase was formed. In this case, the dislocation motion will be the dominated strengthening mechanism. When $f_{Nb} > f_C$, the dominant strengthening mechanism changed to shear banding process instead due to the increased ratio of amorphous phase formed within the regions of GBs in the CuNb alloys.

The physical basis of H–P relationship is intra-granular dislocation interactions or pileups at GBs. However, when grain size decreases to ~50 nm, as in CuNb9.3 at% alloy, dislocations could rarely exist in the grain interiors. In this case, the dominated deformation process should be the full or partial dislocation emission from GBs, glide across the grain interiors and being absorbed by opposite GBs. The resolved shear stress at which a full dislocation (τ_{full}) and two partial dislocations ($\tau_{partial}$) will be emitted from GBs can be calculated as [18]

$$\tau_{full} = \frac{2\alpha Gb}{d} \quad (1)$$

$$\tau_{partial} = \frac{Gb}{3d} + \frac{d-s}{d}\frac{\gamma}{b} \quad (2)$$

where G is the shear modulus, b the Burgers vectors, d the grain size, s the separation distance of two partial dislocations, γ the stacking fault energy, and $0.5 \le \alpha \le 1$. In the present $CuNb_x$ alloy system, the modulus of $CuNb_x$ thin films remained nearly constant with increasing f_{Nb} as shown in Fig. 6. Furthermore, the difference of elasticity modulus between Cu and CuNb9.3 at% was only 8 GPa. In this circumstance, G could be treated as a constant in Eqs. (1) and (2), which predicts a $\tau \sim d^{-1}$ rather than $\tau \sim d^{-1/2}$ dependence which

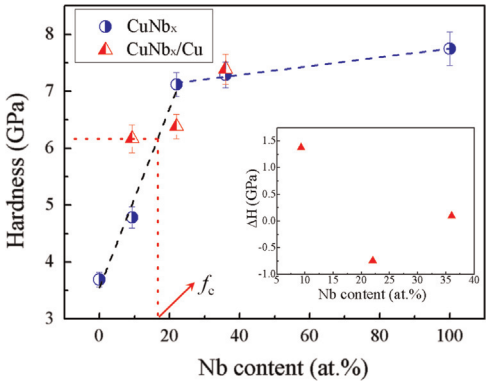

Fig. 4. Comparison of hardness between $CuNb_x$ and $CuNb_x$/Cu samples at various Nb contents. (For interpretation of the references to color in this figure, the reader is referred to the web version of this article.)

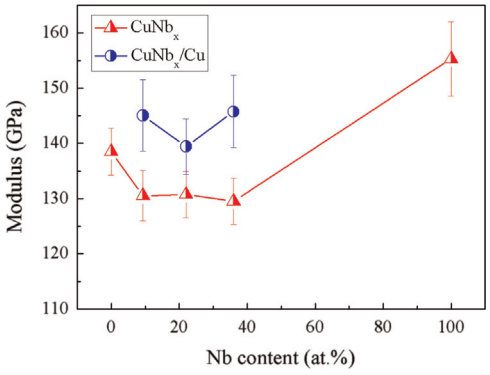

Fig. 6. Elasticity modulus of $CuNb_x$ and $CuNb_x$/Cu samples.

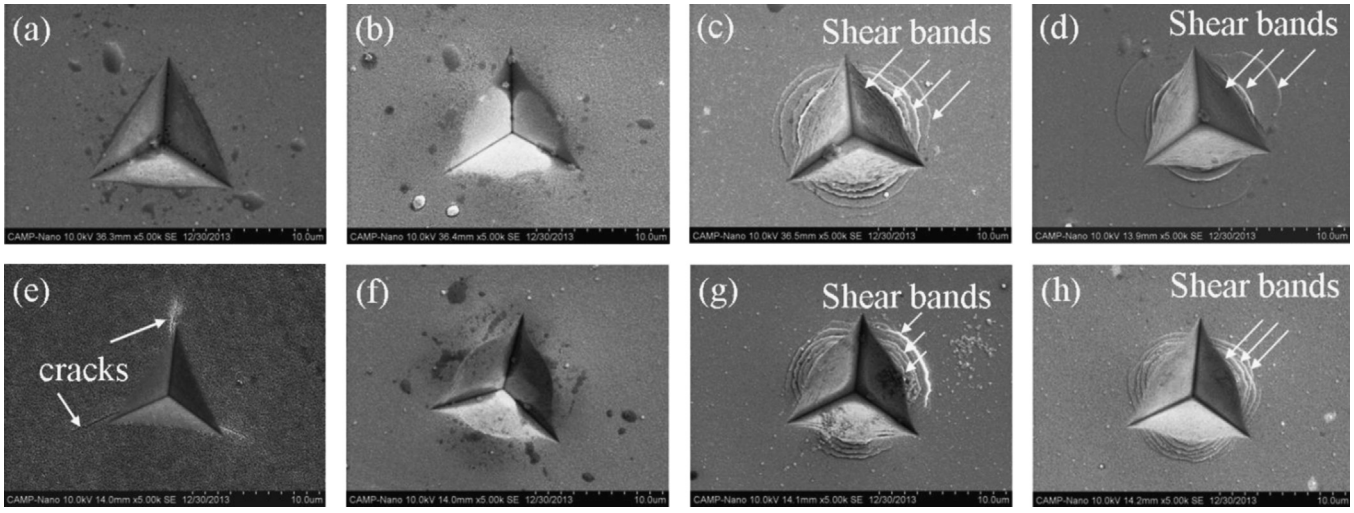

Fig. 5. Indentation morphologies of (a) pure Cu, (b) CuNb9.3 at%, (c) CuNb22 at%, (d) CuNb36 at%, (e) pure Nb, (f) CuNb9.3 at%/Cu, (g) CuNb22 at%/Cu and (h) CuNb36 at%/Cu.

was predicted from dislocation pileup models. For FCC metals, $\tau_{partial}$ is lower than τ_{full} when $d < \sim 50$ nm, which means the deformation mechanism of CuNb alloys should transform from full dislocation emission to partial dislocation emission in a critical grain size d_c. Asaro et al. [19] calculated that d_c for nanocrystalline Cu is about 40 nm. Considering the XRD patterns of CuNb9.3 at% and pure Cu are nearly the same, the dominated strengthening mechanism of CuNb9.3 at% should be full dislocation emission from GBs. Providing the parameters of $G=48.6$ GPa, $b=0.256$, $d=50$ nm, and $\alpha=1$, the upper bound of the resolved shear stress for a full dislocation emission in CuNb9.3 at% is 0.50 GPa according to Eq. (1). The hardness value of 4.18 GPa could be obtained by converting τ to hardness by $H \approx 3.1\sigma$ and $\sigma \approx 2.7\tau$. The calculated value is less than the experimental data of 4.78 GPa, which means that the solid solution effects may also contribute to the strength of CuNb alloys. As a result, the total strength of $CuNb_x$ alloy should be described as

$$\tau = \tau_{dis} + \tau_{ss} \quad (3)$$

where τ_{dis} represents the strengthening effect derived from full or partial dislocation emitted from GBs, and τ_{ss} the strengthening effect derived from the hindering effects of Nb atoms on the motion of an active dislocation.

While $f_{Nb} > f_C$, the strengthening event will be mainly due to the increase of amorphous content along GBs. Under these circumstances, dislocations could hardly emit from GBs and a large number of sliding events occurred in GBs will accommodate the plastic deformation [14]. The results of MD simulations on CuZr nanoglass, the microstructure of which is similar to CuNb36 at% thin film in our study, indicate that the deformation behavior will be undertaken by large number of localized shear banding and the strain within the grains is negligible [20]. As a result, the hardness of CuNb thin films with Nb content higher than f_C exhibited nearly a platform value, which is determined by the Nb content in CuNb amorphous phase. While increasing Nb content close to 100 at%, the hardness of CuNb thin films will be gradually approaching the maximum value of 7.75 GPa that is equal to the hardness of pure Nb as indicated in Fig. 4 by the blue dotted line.

4.1.2. Strengthening mechanism of CuNb/Cu alloy

By adding Cu layers into CuNb alloy, both strengthening and softening effects appeared as Nb content increases, which is quite different from that in CuNb thin films. As mentioned above, three kinds of interface were formed by varying Nb contents, i.e. coherent interface, C/A and A/A mixed interface and totally C/A interface. For coherent interface formed while Nb content is less than f_C, alternating compressive and tensile in-plane stresses existed among neighboring layers which could strongly hinder dislocation movement as depicted in Fig. 7(a). Taking CuNb9.3 at%/Cu as an example, the hardness of the CuNb9.3 at%/Cu was higher than that of CuNb9.3 at% indicating that Cu layers played a reinforcement effect in this composition. The reinforcement effect might derive from the inhibition of full dislocation motion when the dislocations pass through the interface. Then, extra stress is needed to overcome the barrier from alternating in-plane stress and eventually results in the hardness enhancement. It is worth noting that the strengthening effect in CuNb/Cu thin films should mainly derive from the coherent interfaces, and the hardness of CuNb/Cu will maintain a plateau till the interface structure changed. In this case, the value of f_C was evaluated to be about 15.5 at% by examining the intersection of the plateau value of CuNb9.3 at%/Cu and the fitting line of CuNb alloys with Nb content less than 22 at%, as shown in Fig. 4. In addition, the HRTEM image shown in Fig.3(c) indicates that stacking faults were observed in Cu layers, the existence of which may be beneficial to enhance the strength [21].

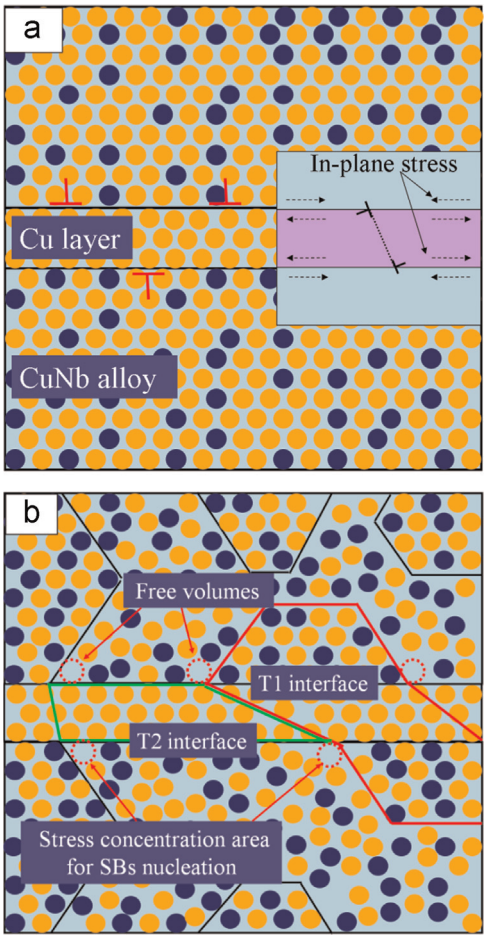

Fig. 7. Schematic diagram of strengthening mechanisms of (a) CuNb9.3 at%/Cu and (b) CuNb22 at%/Cu.

For $f_{Nb} > f_C$, as shear bands were observed in CuNb22 at%/Cu and CuNb36 at%/Cu as shown in Fig. 5, the shear band nucleation and propagation mechanisms will be discussed in the following. For C/A multilayers with the similar amorphous layer thickness as the present $CuNb_x$/Cu thin films, the strength of the amorphous layer has been expressed as the critical stress required for SBs propagation [22]:

$$\sigma = \sqrt{\frac{2\sqrt{2}\,\Gamma E}{h}} \quad (4)$$

where Γ is the SB energy density per unit area, E the measured Young modulus, and h the thickness of the amorphous layer. Other than CuNb22 at%/Cu and CuNb36 at%/Cu, shear bands are also formed in CuNb22 at% and CuNb36 at% alloy thin films as shown in Fig. 5. When the deformation mechanism of all these samples are SBs propagation related, Eq. (4) should be suitable for both CuNb alloy and CuNb/Cu multilayer thin films. When Γ is nearly constant in the identical alloy system and the values of E in all CuNbx alloy thin films are assumed to be identical, the strength of CuNb alloy and CuNb/Cu multilayer thin films is closely related to the parameter h. It is important to note that the value of h should not be the total layer thickness when Eq. (4) is used to predict the strength of monophase $CuNb_x$ alloys. Kim et al. [23] systematically studied the thickness of amorphous layer thickness on the deformation behavior of CuZr/Cu amorphous–crystalline nanolaminates when the thickness of Cu layer was held constant at 16 nm. A critical thickness of about 120 nm for the amorphous layers was identified, over which the strength of the nanolaminates is nearly constant. Furthermore,

the size effects of amorphous layers were considered more important on the deformation behavior, rather than the effects derived from Cu layers or CAIs. Accordingly, the strength of CuNb alloy and CuNb/Cu thin films should be the same when the thickness of CuNb monophase thin films and the CuNb individual layer thickness in CuNb/Cu multilayers is both higher than 120 nm. In the present study, the hardness values of CuNb36 at% and CuNb36 at%/Cu thin films are 7.40 and 7.74 GPa, respectively, indicates that the Cu layers have little effects on the strength of CuNb36 at% alloy, consisted with the observation derived in CuZr/Cu nanolaminates previously [23]. Although the strength is nearly the same for the CuNb36 at% alloy with or without adding Cu layers, the CAIs in CuNb36 at%/Cu strongly affect the distribution of shear bands and will be discussed later.

In the samples with Nb content of 22 at%, the hardness of CuNb22 at%/Cu was 0.74 GPa lower than that of CuNb22 at%, which is inconsistent with the analysis mentioned above, indicating the specific interface structures, i.e., the T1 and T2 interfaces observed in Fig. 3(f) may play a crucial role upon plastic deformation in CuNb22 at%/Cu thin film. For the CuNb/Cu multilayers with f_{Nb} slightly larger than f_C, i.e., CuNb22 at%/Cu, abundant T1 and T2 interfaces existed along the CuNb/Cu interface as depicted in Fig. 7(b), in which Cu layers were divided into numerous discontinuous areas. Furthermore, amorphous area was observed in the present CuNb/Cu multilayers as shown in the inset of Fig. 3(i), which is consisted in the observation in semi-amorphous and amorphous areas in CuNb multilayers [24]. These areas could further interrupt the continuity of the interfaces. This discontinuous structure could result in the inhomogeneous distribution of stress field upon applying external stress. As a result, free volumes that involved in amorphous CuNb phase will accumulate in the interfaces, especially in the corner of Cu layers and CuNb grains connected with them, which result in stress concentration as shown in Fig. 7(b). The deformation mechanism discussed for CuNb36 at% and CuNb36 at%/Cu is based on the SBs propagation process. However, Chen et al. [25] indicated that there is a critical layer thickness below which SBs nucleation dominates the deformation of amorphous layer, above which SBs propagation dominates. Greer et al. [26] indicated that SBs could form in the stress concentration area, in which the SBs could form in a lower average stress but high local stress condition. Under these circumstances, SBs nucleation should dominate the deformation mechanism instead of SBs propagation for crystalline/amorphous multilayers with larger amorphous layer thickness, and eventually results in a lower strength in CuNb22 at%/Cu.

4.2. The morphologies of residual indentations

Enhanced pileups around the residual indentations of pure Cu, CuNb9.3 at% and CuNb9.3 at%/Cu are shown in Fig. 5(a), (b) and (f), respectively. No shear bands appeared around the indentations as NiW NC alloy reported previously [12]. Fig. 8 shows load vs. depth slope as a function of displacement into surface (S vs. D). Specifically, smooth curves corresponding to homogeneous deformation appeared in pure Cu and CuNb9.3 at%/Cu, while distinct troughs corresponding to inhomogeneous deformation appeared in CuNb9.3 at% as indentation depth exceeds 1000 nm. For CuNb9.3 at%/Cu, the coherent interface could prevent dislocation motion and the dislocation will pile up near the interface when the applied stress is relatively low. With increasing applied stress, dislocation could keep moving and pass through the interface to coordinate plastic deformation. This process may inhibit local shear deformation at GBs and leading the CuNb9.3 at%/Cu to be deformed homogeneously. The troughs in S vs. D curve of CuNb9.3 at% should reflect the dislocation multiplication rather than shear bands formation. As discussed earlier, dislocations will pile up at the GBs under the compression process in CuNb9.3 at%. While the density of dislocation reaches a relatively large value, a larger stress will be needed to maintain the plastic deformation. Under this higher stress, more dislocations could nucleate at GBs, and then the plastic deformation became easy. A sudden plastic deformation occurred with the assistance of these dislocations reflecting in the troughs in S vs. D curve.

Despite the pure Cu, CuNb9.3 at% and CuNb9.3 at%/Cu mentioned above, shear bands appeared in both CuNb22 at% and CuNb22 at%/Cu films. The in-plane HRTEM image shown in Fig. 9 indicates that the microstructure of CuNb22 at% is quite similar as observed in fcc metals by molecular dynamics (MD) simulation [27]. For the fcc metal with grain size of 5 nm, specifically, shear banding behavior will occur through the cooperative GB sliding, which is a comprehensive motion of GB sliding, granular rotation and deformation via intergranular slip. The S vs. D curves of these two samples, as shown in Fig. 8(c) and (g), are both abrupt compared to their lower Nb content counterparts, indicating that inhomogeneous deformation occurred in these two samples. However, the curve of CuNb22 at%/Cu presents a comparatively

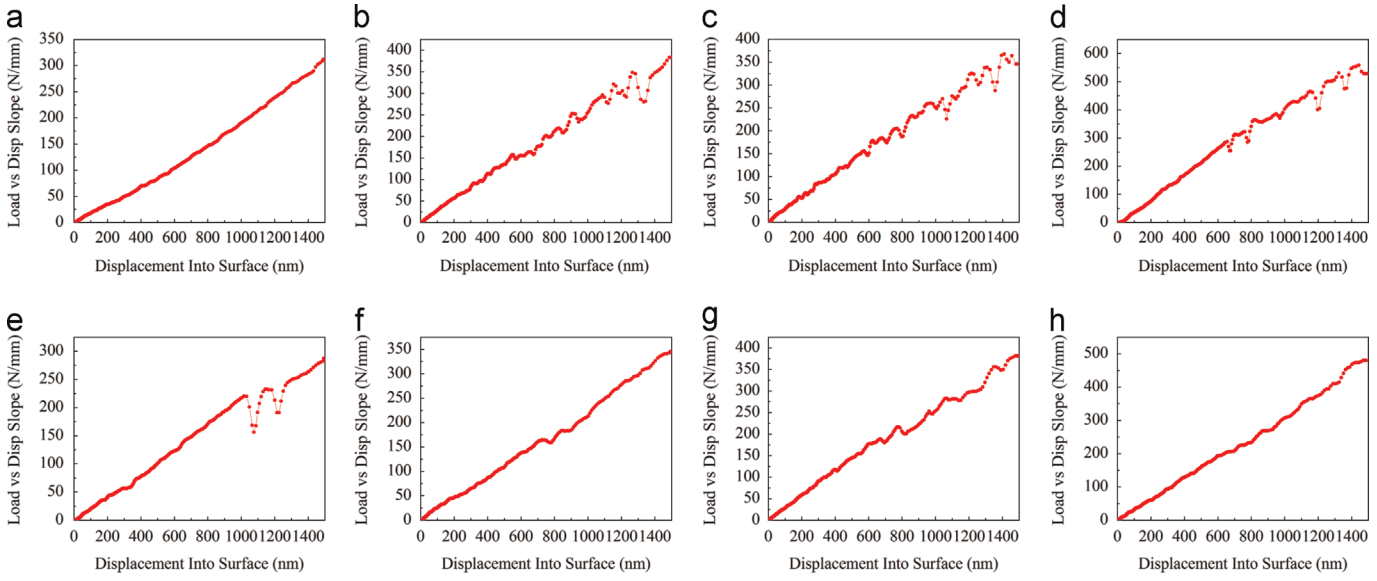

Fig. 8. Load vs. displacement into surface curves of (a) pure Cu, (b) CuNb9.3 at%, (c) CuNb22 at%, (d) CuNb36 at%, (e) pure Nb, (f) CuNb9.3 at%/Cu, (g) CuNb22 at%/Cu and (h) CuNb36 at%/Cu.

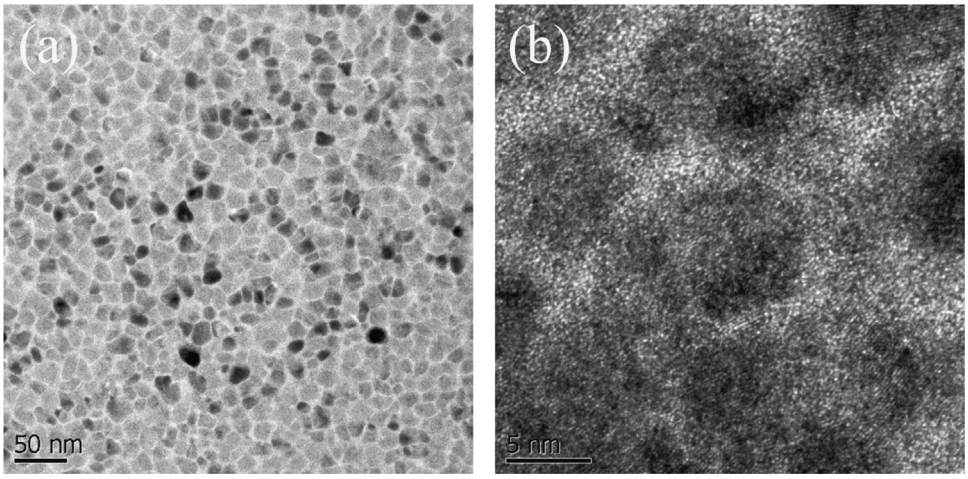

Fig. 9. In-plane HRTEM images of CuNb22 at%.

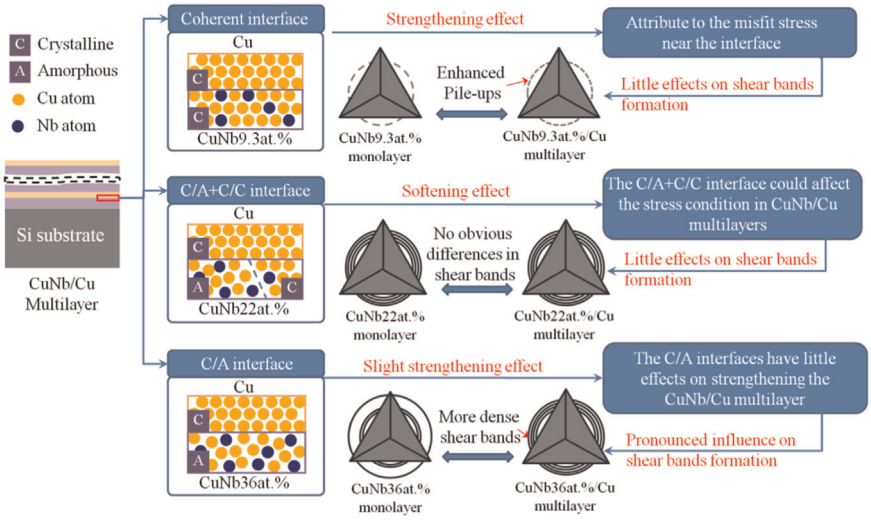

Fig. 10. Schematic diagram of the influence of interface structures on the strengthening mechanism and indentation morphologies of $CuNb_x$/Cu compared with $CuNb_x$ thin films.

smooth tendency due to Cu layer's addition. In CuNb22 at%, shear deformation occurred at the shear plane that formed by cooperative GB sliding, and then shear bands appeared at the indent surface and around the indent edges. Chou et al. [28] indicated that 5 nm layered Ta in ZrCuTi/Ta multilayers could effectively absorb kinetic energy of shear bands and thus reduce the possibility to form SBs as those in monolithic amorphous materials. Similarly, by adding Cu layers into CuNb22 at%, both GBs and stacking faults in Cu layers could facilitate the propagation of shear bands. Then the kinetic energy of shear bands is partially absorbed and the CuNb22 at%/Cu multilayer exhibits homogeneous deformation behavior.

As Nb content increased to 36 at%, the volume fraction of amorphous phase was larger than that of crystalline phase. Then, the deformation behavior was turned to be dominated by amorphous phase, which means that the initiation and propagation of shear bands would facilitated the plastic deformation in the CuNb36 at%. The crystalline grains with grain size of about 2–5 nm were found to successfully inhibit the SBs propagation in Zr55Ti5Al7.5Cu22Ni8Ga2.5 metal glass [29]. However, Eckert et al. [30] point out that there is a critical volume fraction of crystalline phase as a ductile-to-brittle transition is observed. When the grain size of CuNb crystalline grains is 4 nm but the volume fraction of crystalline phase is larger than that in Zr55Ti5Al7.5Cu22Ni8Ga2.5 metal glass, only partial SBs could be inhibited during the compression deformation in CuNb36 at%. As a result, only finite shear bands were observed in the SEM image as shown in Fig. 5(d). By adding crystalline Cu layers, the film was divided into few uniform areas in CuNb36 at%/Cu. The crystalline/amorphous interface in the CuNb36 at%/Cu could effectively resist the motion of local shear bands. Then shear bands cannot pass through the interface, but a shear deformation occurred by the rotation of Cu layers. Then the catastrophic failure by primary shear bands propagation is inhibited. As a result, uniform distribution of shear bands appeared around the indent and the S vs. D curves are more smooth for CuNb36 at%/Cu than CuNb36 at% as shown in Fig. 8(d) and (h). Moreover, macro-cracks, which were mainly formed through local shear bands propagation in amorphous metals, could be effectively inhibited by Cu layers addition.

5. Summary

A comprehensive study of the microstructural features and mechanical properties of both $CuNb_x$ and $CuNb_x$/Cu thin films has been performed by using electron microscopy and nanoindentation techniques, respectively. The experimental observations and their immediate consequences can be summarized as shown in Fig. 10, in which a detailed schematic diagram of the influence of interface

structures on the strengthening mechanism and indentation morphologies of $CuNb_x$/Cu compared with $CuNb_x$ thin films was drew.

By adding crystalline Cu layers, the coherent interface formed in CuNb9.3 at.%/Cu enhance pileup around residual indentation compared with CuNb9.3 at%, while both the samples exhibited no shear banding deformation. In addition, the misfit stress generated via forming coherent interface strengthening hardness of CuNb9.3 at%/Cu multilayers than that of CuNb9.3 at% monolayer. As Nb content increased to 22%, shear bands appeared in both CuNb22 at%/Cu and CuNb22 at% without apparent differences. Moreover, softening occurred by adding Cu layers, as the C/A and C/C interfaces formed in CuNb22 at%/Cu led to the stress concentration, which is beneficial to SBs nucleation. As Nb content increased to 36%, the addition of Cu layers pronounced affect of the shear banding deformation as more and denser shear bands appeared around the residual indentation of CuNb36 at%/Cu than that of CuNb36 at%.

Above all, the various interface structures by adding crystalline layers and altering alloy content could effectively influence the mechanical properties of the nanocrystalline metallic alloy. The potential extension of the aforementioned observations to other metallic alloy systems raises numerous important issues, particularly in achieving metallic alloys with altering combination of both strength and plastic deformation behavior. Moreover, it is of considerable interest to investigate whether this is true for other alloys or is specific to the CuNb alloy used in the present study, and which alloys and the thickness of the added crystalline layers would exhibit optimal mechanical behaviors. The experimental works concerned on those two issues are already underway and will be present in future studies.

Acknowledgments

The present work was supported by the National Natural Science Foundation of China, China (51171141, 51271141, and 51471131) and the Program for New Century Excellent Talents in University, China (NCET-11–0431).

References

[1] J.A. Sharon, H.A. Padilla, B.L. Boyce, J. Mater. Res. 28 (2013) 1539–1552.
[2] Z. Zhang, F. Li, G. Ma, R. Kang, X. Guo, Scr. Mater. 69 (2013) 231–234.
[3] Z.X. Wu, Y.W. Zhang, D.J. Srolovitz, Acta Mater. 57 (2009) 4508–4518.
[4] D. Witkin, Z. Lee, R. Rodriguez, S. Nutt, E. Lavernia, Scr. Mater. 49 (2003) 297–302.
[5] Y. Zhao, T. Topping, J.F. Bingert, J.J. Thornton, A.M. Dangelewicz, Y. Li, W. Liu, Y. Zhu, Y. Zhou, E.J. Lavernia, Adv. Mater. 20 (2008) 3028–3033.
[6] J.Y. Zhang, G. Liu, X. Zhang, G.J. Zhang, J. Sun, E. Ma, Scr. Mater. 62 (2010) 333–336.
[7] A. Misra, J.P. Hirth, R.G. Hoagland, Acta Mater. 53 (2005) 4817–4824.
[8] Y. Wang, J. Li, A.V. Hamza, T.W. Barbee Jr., PNAS 104 (2007) 11155–11160.
[9] A. Donohue, F. Spaepen, R.G. Hoagland, A. Misra, Appl. Phys. Lett. 91 (2007) 241905.
[10] J.Y. Kim, X. Gu, M. Wraith, J.T. Uhl, K.A. Dahmen, J.R. Greer, Adv. Funct. Mater. 22 (2012) 1972–1980.
[11] M. Saber, H. Kotan, C.C. Koch, R.O. Scattergood, Mater. Sci. Eng. A 556 (2012) 664–670.
[12] J.R. Trelewicz, C.A. Schuh, Acta Mater. 55 (2007) 5948–5958.
[13] Y. Liu, D. Bufford, H. Wang, C. Sun, X. Zhang, Acta Mater. 59 (2011) 1924.
[14] Y. Liu, Y. Chen, K.Y. Yu, H. Wang, J. Chen, X. Zhang, Int. J. Plast. 49 (2013) 152.
[15] J.R. Weertman, Mater. Sci. Eng. A 166 (1993) 161–167.
[16] J. Schiøtz, F.D.D. Tolla, K.W. Jacobsen, Nature 391 (1998) 561–563.
[17] T.J. Rupert, J.C. Trenkle, C.A. Schuh, Acta Mater. 59 (2011) 1619–1631.
[18] M.A. Meyers, A. Mishra, D.J. Benson, Prog. Mater. Sci. 51 (2006) 427–556.
[19] R.J. Asaro, S. Suresh, Acta Mater. 53 (2005) 3369–3382.
[20] S. Adibi, Z.D. Sha, P.S. Branicio, S.P. Joshi, Z.S. Liu, Y.W. Zhang, Appl. Phys. Lett. 103 (2013) 211905.
[21] D. Bufford, Z. Bi, Q.X. Jia, H. Wang, X. Zhang, Appl. Phys. Lett. 101 (2012) 223112.
[22] J.Y. Zhang, G. Liu, S.Y. Lei, J.J. Niu, J. Sun, Acta Mater. 60 (2012) 7183–7196.
[23] J.Y. Kim, D. Jang, J.R. Greer, Adv. Funct. Mater. 21 (2011) 4550–4554.
[24] M.N. Polyakov, E. Courtois-Manara, D. Wang, K. Chakravadhanula, C. Kübel, A.M. Hodge, Appl. Phys. Lett. 102 (2013) 241911.
[25] Y. Chen, M.Q. Jiang, L.H. Dai, Int. J. Plast. 50 (2013) 18–36.
[26] A.L. Greer, Y.Q. Cheng, E. Ma, Mater. Sci. Eng. R 74 (2013) 71–132.
[27] A. Hasnaoui, H. Van Swygenhoven, P.M. Derlet, Phys. Rev. B 66 (2002) 184112 (1–8).
[28] H.S. Chou, X.H. Du, C.J. Lee, J.C. Huang, Intermetallics 19 (2011) 1047–1051.
[29] K. Hajlaoui, A.R. Yavari, J. Das, G. Vaughan, J. Alloy. Compd. 434–435 (2007) 6–9.
[30] J. Eckert, J. Das, S. Pauly, C. Duhamel, J. Mater. Res. 22 (2011) 285–301.